Title:
Gaseous nitriding behaviour of 33CrMoV12-9 steel: evolution of the grain boundaries precipitation and influence on residual stress development

Authors:
Sébastien JEGOU[a,x], Laurent BARRALLIER[a], Guillaume FALLOT[b]

Affiliations:
[a] MSMP laboratory, Arts et Métiers ParisTech, 2 cours des Arts et Métiers, 13617 Aix-en-Provence, France, sebastien.jegou@ensam.eu, laurent.barrallier@ensam.eu
[b] Airbus Helicopters, Aéroport International Marseille Provence, 13700 Marignane, France, guillaume.fallot@airbus.com
[x] corresponding author

Highlights:
- The gaseous nitriding behaviour of 33CrMoV12-9 steel was investigated
- A nitrogen supersaturation of ferrite is required for iron nitrides precipitation.
- Carbides transformation is the limiting rate in the supersaturation of ferrite.
- Decrease of residual stresses found origins in the diffusion of the release carbon.
- Transformation kinetics can be controlled by temperature and nitriding potential.

Abstract:
The gaseous nitriding behaviour of 33CrMoV12-9 steel was investigated. The co-diffusion of nitrogen and carbon, precipitation at grain boundaries and mechanical properties evolutions (microhardness, residual stresses) are compared for several nitriding potentials, nitriding time and temperatures. While hardening unequivocally depends on the precipitation of alloying element nitrides MN (M = Cr, V…), the development of residual stresses follows phase transformation kinetics during nitriding. The transformation of carbides into nitrides is the limiting rate in the supersaturation of nitrogen in the ferritic matrix and the diffusion of the released carbon. The lower carbides transformation kinetics the smaller decarburization occurs during nitriding and residual stresses are more compressive. The kinetics is controlled by both the temperature and nitriding potential.

Keywords: (max. 8)
nitriding; steel; diffusion; phase transformation; residual stress

1. Introduction
Toughness of power transmission workpieces is well known to be enhanced by surface strengthening as well as compressive residual stresses [1]. Despite of industrial complications (e.g. process duration, atmosphere control…), gaseous nitriding of steels prevails over other surface treatments of steels by means of lower volumetric distortions of treated parts, higher surface completion and better microstructural (and mechanical) stability in service [2].
Gas nitriding of low alloyed steels consists in the diffusion of nitrogen atoms through the surface of a treated part [3]. Nitrogen is supplied by a surface catalytic decomposition of an ammonia-rich atmosphere at a temperature ranging from 450 to 590 °C. The nitrided case as obtained is usually characterized by a compound layer of iron nitrides (ε)$Fe_{2-3}N$ and/or

(γ')Fe_4N stretching up to 50 µm, and a diffusion zone where a dilute solute diffusion of nitrogen occurs in the ferritic matrix (α)Fe.
In low alloyed steels, the diffusion layer is defined by the precipitation of fine alloying-element nitrides MN (M = Cr, V…) from the reaction of nitrogen with alloying elements either in solid solution in the ferritic matrix or within initial carbides $M_{23}C_6$/M_7C_3 from tempered martensite prior to nitriding [4-7]. Alloying-element nitrides are responsible of both surface strengthening as well as the generation of compressive residual stresses due to volumetric eigenstrains accompanying the precipitation [8-11]. Volumetric eigenstrains are a function of the specific volume of phases as well as changes in the lattice parameters due to chemical composition evolution of phases during nitriding and thermal expansion.
Cementite Fe_3C precipitation occurs at grain boundaries of prior austenite nearly parallel to the nitrided surface [12]. It lies in the carbon release within the ferritic matrix from the transformation of initial carbides into nitrides [5-7]. A co-diffusion of carbon has generally been observed during nitriding [5,13-14]. Depending on the nitriding potential, $K_N = P_{NH3}/P_{H2}^{3/2}$, the carbon atoms diffuse (i) toward the outer surface, leading to decarburization of the material or growth of a carbonitrides (ε)Fe_{2-3}(N,C), and (ii) toward the nitrogen diffusion front, leading to an evolution of initial carbides [3,13-14].
While hardening is unequivocally related to the precipitation of fine alloying elements nitrides [2,4], the development of compressive residual stresses finds origins in the phase transformation kinetics [8-11]. It has been demonstrated to be influenced by the transformation of carbides into nitrides and the subsequent co-diffusion of carbon with nitrogen [5,14-15]. Some authors also referred to a creep phenomenon occurring during nitriding in order to explain the relaxation of residual stresses close to the extreme surface [16-18]. However, a lack of knowledge still exists on the transformation kinetics of carbides and its influence on the development of mechanical properties.
The present work aims investigating the nitriding behaviour of 33CrMoV12-9 steel grade. It focused on chemical and mechanical properties of the diffusion zone. The compound layer has generally been out of interest in industrial applications using the 33CrMoV12-9 steel grade. Carbon diffusion and grain boundaries precipitation were characterized using several nitriding parameters (time, temperature, nitriding potential) and emphasised with the subsequent mechanical response (hardness and residual stresses) of the nitrided cases was studied.

2. Materials and methods

2.1. Material preparation and nitriding treatment

The material of the present work is an industrial 33CrMoV12-9 steel grade. Rectangular samples of 17×13×5 mm^3 were austenitized at 950 °C during 30 min, oil quenched and annealed at 590 °C during 2.5 h. The ASTM grain size of prior austenite was controlled to 8-9 (15.9 to 22.5 µm). Prior to nitriding, specimens were machined on all sides, taken the grease out and finally cleaned using ultrasounds within ethanol.
Gaseous nitriding was performed in a SETSYS Evolution thermogravimetric analyser from Setaram Instrumentation (vertical alumina-made tube furnace and platinum-made suspension). The flow rate in the furnace was set to 200 $mL.min^{-1}$. The nitriding atmosphere was composed of a gas mixture of NH_3-N_2-H_2. Mass-flow controllers adjusted the flow rate of each gas independently. Experimental conditions of gaseous nitriding were varied from 480 and 550 °C during 2.5 to 30 h (Table 1). According to the Lehrer diagram [19], two nitriding

potential were set to 0.33 and 0.79 $atm^{-1/2}$ in the (γ')Fe_4N domain and two others in the (ε)$Fe_{2-3}N$ domain (3.65 and 13.77 $atm^{-1/2}$). These conditions aim exploring nitrided cases with different kinks of compound layers.

2.2. Microstructure characterization

Cross sections of nitrided specimens were grinded and polished up to a 0.5 µm colloidal silica suspension. Observations were performed on a JEOL 7001F scanning electron microscope (SEM) operating at 15 kV and a current of 4 nA equipped with an Oxford Instrument INCA energy-dispersive X-ray detection system (EDX). The backscattered electron mode (BSE) was used for imaging due to a high Z contrast ratio between the matrix and phases at grain boundaries. The surface fraction of phases at grain boundaries was then determined by BSE-SEM image analysis. The surface was subdivided into 20 µm slices for in-depth profiling. Image analysis was performed using the ImageJ package [20]. Discrimination of phases at grain boundaries (cementite or iron nitrides) was made according to on one hand the Z contrast difference between cementite and iron nitrides, and on the other hand by EDX analysis. The procedure was used for qualitative estimation of the fraction of precipitates at grain boundaries and the error made by image analysis on BSE-SEM micrographs was not estimated in the present work.

2.3. Chemical analysis

Nitrogen and carbon contents were determined by optical emission spectrometry using a Spectro SPECTROMAXx MX5M BT. Four analyses were performed on four different areas without any overlapping on each nitrided surface. After each analysis, the size of area analysed is of nearly 0.5 mm diameter by 30 µm in depth. Depth profiling is obtained by successive mechanical grinding until elimination of previous sparks. Layer removal was controlled by dial indicator.

2.4. Mechanical characterization

The present work focused on mechanical properties of the diffusion zone defined by a ferritic matrix α-Fe. This is the reason why in-depth profiles start at 50 µm below the outer surface
Hardness was obtained using a Leica VMHT device with a load of 2 N during 15 s. The effective depth of nitriding is defined as the core hardness plus 100 HV 0.2.
X-ray analysis was carried out on a Siemens D500 diffractometer equipped with a linear detector and Cr-K_α radiation (giving a penetration depth of approximately 6.5 µm). Residual stress analyses were performed on the {211} diffracting plane of α-Fe. The $\sin^2\psi$ method was used to determine the mean residual stresses (σ_{xx} - σ_{zz}) in α-Fe along the nitriding depth *z* [21]. X-ray elastic constants were calculated from α-Fe elastic constants using a Kröner-Eshelby model ($S_1^{\{211\}} = -1.25.10^{-6}\ \mathrm{MPa}^{-1}$; $\frac{1}{2}S_2^{\{211\}} = 5.85.10^{-6}\ \mathrm{MPa}^{-1}$) [22]. Electro-chemical surface layer removal (controlled by dial indicator) was carried out using a Struers Lectropol 5 device for in-depth profiling. Residual stress profiles were finally corrected from successive layer removal using the modified Moore and Evans approach [23-24].

3. Results

3.1. Microstructure

3.1.1. The compound layers

The first 75 µm of the nitrided cases were observed by scanning electron microscopy. The backscattered electron mode (BSE) was used in order to distinguish iron carbides from iron nitrides at grain boundaries of prior austenite grains. According to the atomic numbers of elements and composition of iron nitrides ((ε)$Fe_{2-3}N$ and (γ')Fe_4N) and carbides (Fe_3C cementite), nitrides bring out darker than carbides on SEM-BSE micrographs. EDX mapping was also used to confirm observations (Figure 0).
Depending on the nitriding potential, different kinds of nitrided surfaces are observed at 550 °C (Figures 1 and 2). At 0.33 $atm^{-1/2}$, no compound layer is present except after 5 h of nitriding where (γ')Fe_4N nucleated on several areas. When increasing the nitriding potential, a compound layer developed and is composed of iron nitrides (ε)$Fe_{2-3}N$ and (γ')Fe_4N as confirmed by XRD analysis (Figures 3 and 4). The higher nitriding potential, the thicker the compound layer is.
For a given nitriding potential of 3.65 $atm^{-1/2}$, a compound layer systematically developed between 480 and 550 °C. The higher temperature the thicker the compound layer is (Figures 5 and 6). After 30 h of nitriding, the precipitation of iron nitrides from grain boundaries and prior martensite laths is less pronounced when the temperature increases (Figure 6). The compound layers are characterized by iron nitrides (ε)$Fe_{2-3}N$ and (γ')Fe_4N as confirmed by XRD analysis (Figures 7 and 8).
The nitrides surfaces are characterized by a thin porous and brittle layer at the outer surface composed of mainly (ε)$Fe_{2-3}N$. The thickness of this layer increases when nitriding parameters increase, i.e. when the nitrogen content is closed to equilibrium with the NH_3-rich atmosphere (recombination of N as N_2 [2]).

3.1.2. Grain boundary precipitation

According to the transformation of initial carbides (M_7C_3/$M_{23}C_6$ (M = Cr, Mo…)) into nitrides MN (M = Cr, V, Mo…) [6-7], the precipitation at grain boundaries nearly parallel to the nitrided surface is composed of cementite Fe_3C as shown in Figure 0. Depending on nitriding conditions, grain boundaries can be connected to the compound layer and composed of iron nitrides as confirmed by BSE-SEM micrographs and EDX analysis (Figure 0). Due to the low volume fraction of precipitates, no X-ray analysis was performed to identified the nature of iron nitrides at grain boundaries in the present study. However, previous work concluded on the presence of (γ')Fe_4N at grain boundaries at the interface between the compound layer and the diffusion zone [13].

Figure 9 gives the depth where the porous and dense layers (both defining the compound layer (see Figure 5 for instance)), iron nitrides (Fe_xN) and a mixture of iron nitrides plus carbides (Fe_xN +Fe_3C) at grains boundaries are observed based on BSE-SEM observations and EDX analyses. The error made on the given depth is estimated to less than half of the grain size (< 10 microns). After 30 h at 550 °C, the presence of iron nitrides at grains boundaries extends to deeper depths when decreasing the nitriding potential (Figure 9.a) whereas the thickness of the compound layer decreases. At a potential of 3.65 $atm^{-1/2}$ and after 30 h, a temperature elevation involves a growth of the compound layer and the presence of iron nitrides deeper in the diffusion zone (Figure 9.b). The presence of iron nitrides at grain boundaries progresses at deeper depths with the duration of nitriding (Figure 9.c).

Figure 10 gives the surface percentage of phases (from BSE-SEM image analyses) present at grain boundaries through the diffusion layer. The compound layer was not considered in image analysis. Profiles generally exhibit an evolution of the fraction of carbides at grain boundaries divided in four zones such at 550 °C in Figure 10.b: (i) an extreme surface (from 10 to 60 µm) characterized by a decrease of the fraction of precipitates at grain boundaries, (ii) an increase of the fraction from a minimum close to the surface to a maximum at a deeper depth, (iii) a plateau at the maximum fraction and (iv) a precipitation decrease at grain boundaries until no carbides can be detected by SEM at deeper depth. Depending on nitriding conditions, zone (i) or (ii) are not observed (see Figure 10.c (0.33 $atm^{-1/2}$) and 10.b (480 °C) respectively). The gradient of zone (ii) is more pronounced when decreasing the nitriding potential (Figure 10.a). The level of the plateau of zone (iii) decreases with a temperature elevation from 480 to 550 °C (Figure 10.b) but increases with the nitriding potential from 0.33 to 0.79 $atm^{-1/2}$ (Figure 10.a). The maximum fraction and plateau extent within the depth are similar for both 0.79 and 3.65 $atm^{-1/2}$ nitriding potentials at 550 °C and 30 h nitriding. The fraction of precipitates at grain boundaries also evolves during nitriding as observed on Figure 10.c at 550 °C. For instance, at a given depth of 60 µm and K_N = 0.33 $atm^{-1/2}$, the fraction of precipitates at grains boundaries increases to a maximum before decreasing for longer nitriding.
Despite of a similar extent of the presence of both iron nitrides and carbides at grain boundaries at 550 °C (Figure 9.a), the use of a nitriding potential of 0.79 $atm^{-1/2}$, in the (γ')Fe_4N domain according to the Lehrer diagram, involves a lower precipitation at grain boundaries of the first 60 µm of the diffusion zone than for 3.65 $atm^{-1/2}$.

3.2. Content in-depth profiles

The nitrogen and carbon content in-depth profiles are given in Figures 11 and 12 respectively. The enrichment and diffusion kinetics of nitrogen are consistent with the influence of nitriding parameters, i.e. they increase with the temperature and time of nitriding. They are governed by the formation of a compound layer as shown in Figure 11.c where nitrogen content profiles are all similar when $K_N \geq 0.79$ $atm^{-1/2}$ for which compound layers were observed (Figures 1, 2, 5 and 6). In case of a nitriding potential of 0.33 $atm^{-1/2}$, where no compound layer developed after 30 h at 550 °C (Figure 2), the enrichment of nitrogen reaches 1.20 wt.%. Some profiles exhibit an increase of nitrogen below the compound layer when a fraction of nitrogen close to 1.3 wt.% is reached. The corresponding depth is concomitant with the presence of both iron nitrides and carbides at grain boundaries (Figure 9).

The carbon diffusion kinetics with nitriding conditions is given in Figure 12. All nitrided cases are characterized by a diffusion of carbon toward the outer surface and at the nitrogen diffusion front. The decarburization of the surface is limited when decreasing the temperature and for short nitriding as well as when the potential of nitriding increases. The carbon enrichment at the outer surface increases with the nitriding potential at 550 °C and 30 h of nitriding. This is related to the presence of a porous and brittle compound layer ((ε)$Fe_{2-3}N$) observed in Figure 2. Carbon content profiles are characterized by a constant level of nearly 0.23 wt.% through the diffusion layer after 30 h at 550 °C in agreements with the maximum plateau of precipitates at grain boundaries (zone (iii) in Figure 10.b). This is attributed to the transformation kinetics of initial carbides into nitrides closed to a steady state during nitriding

(Figure 12.d). When the temperature decreases, the carbides transformation rate also decreases leading to a lower diffusion of carbon into the ferritic matrix (Figure 12.b). It corresponds to an increase of the maximum level of precipitates at grain boundaries (Figure 10) and a shorter extent of the presence of nitrides at grains boundaries (Figure 9). The diffusion of carbon at the nitrogen diffusion front involves an enrichment of carbon that increases with the nitriding conditions.

3.3. Hardness profiles

The hardness in-depth profiles are given in Figure 11. Hardening is related to the precipitation of alloying elements nitrides MN (M = Cr, V …) finely dispersed into the ferritic matrix, and thus to the content and diffusion of nitrogen through the treated surface. No correlation is observed between the evolution of hardness with the evolution of precipitation at grain boundaries. It follows that hardening of a nitrided case is enhanced, in one hand, when the nitrogen content increases, and in the other hand, at low temperature and for short nitriding that prevent from growth and coarsening of precipitates. An exception occurs at 480 °C in case of which hardening increases with the nitriding time but can be explained by a non-complete precipitation of nitrides close to the surface after only 5 h as suggested by the increase of the nitrogen content with time in the first hundred microns. Because the nitrogen content increases at deeper depth below the surface, the effective depth is enhanced with the temperature and time of nitriding. However, the level of hardening remains lower deeply below the surface than at the close surface due to incomplete precipitation of nitrides, a lower nitrogen flux that involves growth/coarsening of existing precipitates rather than the nucleation of new ones and finally due to an increase of initial carbides according to the enrichment of carbon in front of the nitrogen diffusion front [5,13].

3.4. Residual stress profiles

Figure 12 shows the in-depth residual stress profiles obtained from XRD analyses. Profiles are characterized by compressive residual stresses according to positive volumetric eigenstrains accompanying the precipitation of alloying elements nitrides within the ferritic matrix. MN nitrides (M = Cr, V…) are indeed characterized by a higher specific volume than the ferritic matrix (10.7 and 7.1 $cm^3.mol^{-1}$ respectively) [2,13].
It can be observed that the higher the temperature the lower compressive residual stresses are. Indeed, after 5 h and 3.65 $atm^{-1/2}$, the maximum compressive residual stresses are found close to -1550 MPa at 480 °C but only -600 MPa at 550 °C. The magnitude of compressive residual stresses also decreases with the duration of nitriding at a given nitriding potential. Because of the interdependence with the diffusion of nitrogen, the location of the maximum compressive residual stresses and the extend of the residual stress state are found at deeper depth when increasing the temperature and time of nitriding. A significant difference can be observed in the case of a 0.33 $atm^{-1/2}$ potential for which the lower extent of the stress in-depth profile is related to a lower nitrogen diffusion (Figure 11).
Compressive residual stresses evolve non-negligibly close to the surface at the beginning of nitriding. For instance, at a 50 µm depth, residual stresses decrease from -1600 (5 h) to -1100 (30 h) MPa at 480 °C, -1100 (5 h) to -350 (30 h) MPa at 520 °C and from -450 (5 h) to -200 (30 h) MPa at 550 °C. After 5 h, decrease of compressive residual stresses below the maximum

residual stresses already occurred at 50 µm at 550 °C, whereas compressive residual stresses were still maintained to a maximum close to the surface at 480 °C after 30 h.
The evolution of the maximum of compressive residual stresses at 550 °C and a 3.65 $atm^{-1/2}$ nitriding potential tends to be limited when a steady state in the diffusion of carbon appear to be reached (Figure 12.d).

4. Discussion

4.1. Diffusion kinetics

Considering a semi-infinite plate of normal axis z, the characteristic diffusion depth z_{eff} can be approximate to [25-26]:

$$z_{eff} \approx \sqrt{2D_N^{\alpha-Fe}t} \quad (1)$$

where t is the time and $D_N^{\alpha-Fe}$ the diffusion coefficient of nitrogen in the ferritic matrix. The diffusivity is assumed independent of the concentration as a function of the depth.
Equalling the characteristic diffusion depth to the effective depth of nitriding (defined as the depth where hardness corresponds to the core hardness plus 100 HV 0.2 (Figure 11)), the effective diffusion coefficient of nitrogen in the ferritic matrix can be calculated adopting an Arrhenius-type temperature dependence in the 480-550 °C range:

$$D_N^{\alpha-Fe} = D_{o,N}^{\alpha-Fe} exp\left(\frac{-E_N^{\alpha-Fe}}{RT}\right) \quad (2)$$

where $D_{o,N}^{\alpha-Fe} = 1.24.10^{-3}$ (cm^2/s) and $E_N^{\alpha-Fe} = 74,,9$ (kJ/mol) the activation energy for diffusion in the ferritic matrix, R the universal gas constant and T the temperature.
Following a similar approach, and defining the characteristic diffusion depth by the depth of the maximal concentration in front of the nitrogen diffusion front (Figure 12), the diffusion coefficient of carbon in the ferritic matrix is found in the 480-550 °C range:

$$D_C^{\alpha-Fe} = D_{o,C}^{\alpha-Fe} exp\left(\frac{-E_C^{\alpha-Fe}}{RT}\right) \quad (3)$$

where $D_{o,C}^{\alpha-Fe} = 1.89.10^{-5}$ (cm^2/s) and $E_C^{\alpha-Fe} = 37{,}0$ (kJ/mol).
Despite of the precipitation of alloying elements nitrides MN (M = Cr, V…), the diffusivity of nitrogen in the ferritic matrix compares well with the diffusivity of nitrogen in iron [27-28]. The activation energy for carbon diffusion in the ferritic matrix is however twice less than in the literature and the diffusivity is found 8 to 4.5 times higher than in the literature at 480 and 550 °C respectively [28]. This has to be emphasized with the decarburization of the close surface due to the gas atmosphere, the enrichment of carbon in front of the nitrogen diffusion front and the precipitation of cementite at grain boundaries through the diffusion zone. On one hand, the higher diffusivity of carbon can be explained by a higher activity of nitrogen with alloying elements that are initially present in both the ferritic solid solution and carbides. It suggests a higher activity of carbon in free-nitrogen material. As a consequence, the diffusion of nitrogen atoms leads to the observed enrichment of carbon in front of the nitrogen diffusion front. On the other hand, the increase of carbon diffusivity in α-Fe with the decrease of the nitriding temperature reflects the lower activity of carbon with the gas atmosphere at low temperature leading to a less pronounced decarburization of the close surface (Figure 12).

4.2. Precipitation at grain boundaries

The fraction of precipitates at grain boundaries and nitrogen and carbon contents through the diffusion zone are given in Figure 13.

The depth where cementite is observed at grain boundaries from SEM-BSE micrographs is located between the beginning of the carbon plateau and the carbon enrichment at the nitrogen diffusion front. The fraction of carbides at grain boundaries then increases according to the increase of the nitrogen content. It corresponds to the transformation of initial carbides into alloying element nitrides with a release of carbon atoms into the ferritic matrix that diffuse either at grain boundaries or in front of the nitrogen diffusion front.

For short nitriding (5 h at 550 °C, K_N = 3.65 $atm^{-1/2}$, Figure 13.b), a continuous augmentation of the fraction of precipitates at grain boundaries with the nitrogen content is observed. When nitrogen reaches nearly 1.2 wt.% at 55 µm below the surface, the fraction of precipitates at grains boundaries is maximum and equal to 3.1 surf.%. For higher nitrogen content (up to 1.3 wt.% at the surface), the carbon content decreases as well as the fraction of precipitates at grain boundaries. Iron nitrides is observed at grain boundaries up to 30 µm below the surface on BSE-SEM micrograph (Figure 9). After 30 h (Figure 13.c), the nitrogen enrichment increases as well as the fraction of carbides at grains boundaries (maximum of 3.3 surf.% from 1.0 to 1.2 wt.% nitrogen) whereas more pronounced decarburization occurred. Iron nitrides is observed at grain boundaries up to 55 µm below the surface on BSE-SEM micrograph (Figure 9) when the nitrogen content is higher to 1.3 wt.%. It suggests that, on one hand, the complete transformation of initial carbides into alloying elements nitrides and cementite was not yet reached after 5 h in the diffusion zone for nitrogen below 1.2 wt.%, and on the other hand, a transformation of cementite into iron nitrides occurs at the interface between the compound layer and diffusion zone.

The fraction of precipitates at grain boundaries reaches a maximum level of 3.3 surf.% characterized by a certain extent within the diffusion zone. It is in agreements with the carbon plateau after 30 h at 550 °C for 0.79 and 3.65 $atm^{-1/2}$ (Figures 13.c and 13.d), as well as a nitrogen content increasing from 1.0 to 1.2 wt.%. When nitrogen continues to increase, the quantity of precipitates at grains boundaries decreases in agreements with the decrease of the carbon content. Nitrogen higher than 1.3 wt.% is in correlation with the observation of iron nitrides at grain boundaries and the overall fraction of precipitates at grain boundaries depends on the carbon content. It is higher after 30 h at 550 °C for high nitriding potential (3.65 $atm^{-1/2}$, (ε)$Fe_{2-3}N$ domain) than for a (γ')Fe_4N nitriding potential (0.79 $atm^{-1/2}$). For 0.33 $atm^{-1/2}$ nitriding potential ((γ')Fe_4N domain) at 550 °C and after 30 h, the maximum nitrogen content was measured close to 1.2 wt.%, below the threshold (1.3 wt.%) that corresponds to the observation of iron nitrides at grains boundaries in the present study. Between 1.0 and 1.2 wt.%, a decrease of the fraction of precipitates at grains boundaries is observed rather than a constant fraction as compared to higher nitriding potential. It suggests that when the nitriding potential decreases, carbon predominantly diffuses toward the outer surface due to a higher activity of carbon with the gas mixture at the gas-solid interface.

For low temperature nitriding (30 h, 480 °C, K_N = 3.65 $atm^{-1/2}$, Figure 13.a), a continuous augmentation of the fraction of precipitates at grain boundaries with the nitrogen content (up to 1.3 wt.%) is observed. Between 1.0 and 1.2 wt.% nitrogen, the fraction of precipitates at grain boundaries increases from 2.8 to 4 surf.% that is the maximum of precipitates observed in the present study. It is associated to almost no carbon redistribution within the diffusion zone. Higher than 1.2 wt.%, the carbon content tends to decrease and iron nitrides is observed

at grain boundaries with carbides (Figure 9) when 1.3 wt.% nitrogen is reached. It suggests that the carbides transformation kinetics is slower at 480 than 550 °C and that the released carbon in the ferritic matrix segregate at grain boundaries to form cementite rather than diffuses at the outer surface or nitrogen diffusion front.

4.2. Residual stresses

The generation of residual stresses during nitriding finds origins in volumetric eigenstrains that accompany the precipitation of alloying elements nitrides in the ferritic matrix (specific volume of 10.7 and 7.1 $cm^3.mol^{-1}$ respectively). Depending on the fraction of nitrogen that reacts with alloying elements initially in the ferritic solid solution or tempering carbides ($M_7C_3/M_{23}C_6$), volumetric eigenstrains can fluctuate between 51 and 22 % respectively [2,13]. Therefore, the development of compressive residual stresses depends on the kinetics of the carbides transformation during nitriding. The effect of thermal stress has usually been assumed negligible due to slow cooling after nitriding.
The maximum compressive residual stresses are measured at 480 °C for a nitriding potential of 3.65 $atm^{-1/2}$ when the precipitation of alloying elements nitrides is maximal (nitrogen higher than 1.0 wt.% that is the maximum fraction of nitrogen that can react with alloying elements to form MN nitrides (M = Cr, V…) in the studied steel grade) as well as the fraction of carbides at grain boundaries, i.e. when the diffusion of carbon is limited in the diffusion zone.
When the kinetics of carbides transformation into alloying elements nitrides increases (such as when the nitriding temperature increases), a more pronounced diffusion of the released carbon occurs either toward the outer surface or at the nitrogen diffusion front. It results in a decrease of the total amount of precipitates (alloying elements nitrides plus carbides) through the diffusion zone, and so lower volumetric eigenstrains, that consequently involves a decrease of compressive residual stresses such as at 520 °C (Figure 12.a).
When residual stress in-depth profiles exhibit a maximum of residual stresses such as at 550 °C, the maximum compressive residual stresses depth corresponds to a nitrogen content superior to 1.0 wt.%, that is the maximum fraction of nitrogen that can react with alloying elements to form MN nitrides (M = Cr, V…) in the studied steel grade. If the nitrogen enrichment of the diffusion zone continues (> 1.0 wt.%), a decrease of compressive residual stresses closed to the surface is observed. With respect to the decrease of the carbon content (released from the transformation of carbides) and fraction of precipitates at grain boundaries during nitriding, it corresponds to the generation of negative volumetric eigenstrains that involve a decrease of compressive residual stresses.
The maximum compressive residual stresses tend to decrease when the duration of nitriding increases (-900 to -600 MPa from 2.5 to 30 h nitriding at 550 °C and K_N = 3.65 $atm^{-1/2}$ in Figure 12). It is in correlation with the continuous decrease of carbon within the diffusion zone from the continuous transformation of carbides. It tends toward an asymptote when a steady state in the transformation of carbides tends to be reached.
The carbon enrichment in front of the nitrogen diffusion front is also of interests because it increases the fraction of initial carbides ($M_7C_3/M_{23}C_6$ (M = Cr, Mo…)), to be transformed later into alloying element nitrides and cementite, and decrease the fraction of alloying elements available in the ferritic solid solution. The transformation leads then to lower positive volumetric eigenstrains and less compressive residual stresses [13,15].

4.3. Carbides transformations

Present results suggest a continuous transformation of carbides into nitrides that qualitatively occurs during nitriding as follows: (1) transformation of initial carbides (M_7C_3/$M_{23}C_6$) into alloying elements nitrides MN (M = Cr, V, Mo…) and cementite at grain boundaries and (2) transformation of cementite into iron nitrides at grain boundaries.
Both transformations release carbon into the ferritic matrix that diffuses either toward the outer surface or at the nitrogen diffusion front. They are responsible for the continuous decarburization of the nitrided surfaces. For short nitriding, or at the interface between the compound layer and the diffusion zone during nitriding, the diffusion of carbon in either direction depend on the nitriding potential and the growth kinetic of the (ε)$Fe_{2-3}N$ iron nitride layer on top of the treated surface. (ε)$Fe_{2-3}N$ iron nitride is characterized by a large solubility limit of carbon limiting decarburization of the surface [3]. The equilibrium of flux in both direction leads to a minimum of carbon content below the compound layer.
During nitriding, the transformation of carbides into nitrides appears to reach a steady state leading to a constant level of carbon through the diffusion zone. Although residual stresses find origins in the precipitation of alloying elements nitrides; the extend of the maximum level and the amplitude of residual stresses are in close relation with the extent and amplitude of the level of carbon. The reduction of compressive residual stresses is in agreements with the continuous transformation of carbides as well as the decrease of the volume fraction of precipitates at grain boundaries due to the diffusion of the continuous released carbon into the ferritic matrix.
When nitrogen atoms have fully reacted with alloying elements to form nitrides MN (M = Cr, V…), i.e. nitrogen higher than 1.0 wt.%, kinetics of carbides transformations (cementite into iron nitrides), and development of residual stresses, should actually depend on the displacement of irons atoms and consequently on the characteristic diffusion distance *L* of iron atoms in ferrite $L = (2.D.t)^{1/2}$ [26,29]. Figure 14 shows that the evolution of residual stresses and both nitrogen and carbon contents at 50 µm below the surface and at the depth of the maximum compressive residual stresses are in good agreements with the characteristic diffusion distance of iron atoms in ferrite. The change in the evolution of residual stresses at these two characteristic depths is in correlation with a nitrogen content that reached 1.2 wt.% and a higher loss of carbon. It can thus be concluded that the development of residual stresses during nitriding depends on the kinetics of the transformation of cementite into iron nitrides that is the limiting rate in the nitrogen supersaturation of the ferritic matrix.
It is noted that iron nitrides can only be observed at grain boundaries for depth where the nitrogen content exceed 1.3wt.% at the beginning of the diffusion zone below the compound layer. The transformation of cementite may so lead to either a transformation into an $Fe_3(C,N)$ phase, such a transformation being crystallographically possible [30], and identified as a carbide due to the main presence of carbon, or a precipitation of a (M_xFe_{1-x})N (M = Cr, V…) phase [31-32] that corresponds to an increase of the nitrogen solubility limit into the distorted (to the fcc arrangement of (γ')Fe_4N) ferritic matrix surrounding MN nitrides leading to the precipitation of iron nitrides when the maximum supersaturation of nitrogen is reached (close to 1.3 wt.% according to the results of the present work and steel grade).
The present results confirm that the development of residual stresses during nitriding is a function of the carbides transformation kinetics and not of a creep phenomenon as assumed by some authors in the literature in order to be able to model the decrease of residual stresses, especially below the compound layer at the beginning of the diffusion zone [16-18]. The

corresponding authors did not consider the complex kinetics of the transformation of carbides in their works.
Finally, in order to keep high compressive residual stress during nitriding, one must, firstly, promote the precipitation of cementite by limiting the diffusion of carbon atoms released during the transformation of initial carbides (low temperature, high nitriding potential), and secondly, limit the transformation of cementite into iron nitrides and so the nitrogen supersaturation of the matrix in order to save the treated surface from the carbon diffusion and decrease of the volume fraction of precipitates. The last can be performed during the process by decreasing the nitriding potential in a multi-steps nitriding [33].

5. Conclusions

The nitriding behaviour of 33CrMoV12-9 steel was investigated for several nitriding conditions including different nitriding potentials, temperatures and durations of gaseous nitriding. The continuous transformation of carbides (M_7C_3/$M_{23}C_6$ and cementite) into nitrides (MN and (ε)$Fe_{2-3}N$/(γ')Fe_4N) was highlighted. It results in a continuous decarburization and diffusion of carbon into the diffusion zone during nitriding. The lower nitriding potential and the higher temperature, the more pronounced the decarburization is. The higher activity of nitrogen with alloying elements involves a lower energy for carbon diffusion in the ferritic matrix than expected and leads to the observed enrichment of carbon in front of the nitrogen diffusion front. The kinetics of the transformation of carbides qualitatively involves two steps of transformation: initial carbides firstly transforms into alloying elements nitrides and cementite at grain boundaries, and secondly, cementite transforms into iron nitrides. The supersaturation of nitrogen required to observe the precipitation of iron nitrides depend on the kinetics of the transformation of carbides. The higher kinetics of transformation, the faster the supersaturation of nitrogen is reached leading to the precipitation of iron nitrides at grain boundaries. The evolution of residual stresses during nitriding follows the kinetics of the transformation of carbides and the released carbon free to diffuse. Compressive residual stresses develop during nitriding until the precipitation of alloying elements nitrides has fully occurred (from both the solid solution and initial carbides). When the continuous transformation of cementite takes place, the diffusion of the released carbon involves a decrease of the volume fraction of precipitates and compressive residual stresses decrease because of negative volumetric eigenstrains. The continuous transformation of cementite is obvious during nitriding but the product of such transformation must be explored in more details.

Figure 0: EDX mappings at the interface between the compound layer and the diffusion zone. Sample nitrided at 520 °C during 30 h for K_N = 3.65 $atm^{-1/2}$.

Figure 1: Backscattered electron micrographs of a 33CrMoV12-9 steel nitrided during 5 h at 550 °C and (a) 0.33, (b) 0.79, (c) 3.65 and (d) 13.77 $atm^{-1/2}$.

Figure 2: Backscattered electron micrographs of a 33CrMoV12-9 steel nitrided during 30 h at 550 °C and (a) 0.33, (b) 0.79, (c) 3.65 and (d) 13.77 $atm^{-1/2}$.

Figure 3: XRD analyses of the surface of a 33CrMoV12-9 steel nitrided during 5 h at 550 °C and a nitriding potential of 0.33, 0.79, 3.65 and 13.77 $atm^{-1/2}$.

Figure 4: XRD analyses of the surface of a 33CrMoV12-9 steel nitrided during 30 h at 550 °C and a nitriding potential of 0.33, 0.79, 3.65 and 13.77 $atm^{-1/2}$.

Figure 5: Backscattered electron micrographs of a 33CrMoV12-9 steel nitrided during 5 h at 3.65 $atm^{-1/2}$ and (a) 480, (b) 520 and (c) 550 °C.

Figure 6: Backscattered electron micrographs of a 33CrMoV12-9 steel nitrided during 30 h at 3.65 $atm^{-1/2}$ and (a) 480, (b) 520 and (c) 550 °C.

Figure 7: XRD analyses of the surface of a 33CrMoV12-9 steel nitrided during 5 h at 3.65 $atm^{-1/2}$ and a temperature of 480, 520 and 550 °C.

Figure 8: XRD analyses of the surface of a 33CrMoV12-9 steel nitrided during 30 h at 3.65 $atm^{-1/2}$ and a temperature of 480, 520 and 550 °C.

Figure 9: Comparisons of the depths where the porous ((ε)$Fe_{2-3}N$) and dense ((γ')Fe_4N) layers, iron nitrides (Fe_xN) and a mixture of iron nitrides plus carbides (Fe_xN +Fe_3C) are observed at grain boundaries through the diffusion layers of nitrided 33CrMoV12-9 steel.

Figure 10: Surface percentage of phases at grains boundaries from BSE-SEM image analyses of nitrided 33CrMoV12-9 steel.

Figure 11: Nitrogen content and hardness in-depth profiles of a 33CrMoV12-9 steel nitrided for various conditions.

Figure 12: Carbon content and residual stress in-depth profiles of a 33CrMoV12-9 steel nitrided for various conditions.

Figure 13: Comparisons between nitrogen/carbon in-depth chemical analysis and the fraction of precipitates at grains boundaries of a 33CrMoV12-9 steel nitrided for various conditions.

Figure 14: (a) Residual stresses, (b) carbon and (c) nitrogen contents as a function of the characteristic diffusion distance of iron in the ferritic matrix at 50 µm below the surface and

at the depth of the maximum compressive residual stresses. The nitriding potential is equal to 3.65 $atm^{-1/2}$.

[1] D. Girodin, Deep nitrided 32CrMoV13 steel for aerospace bearings applications, NTN Technical Review 76 (2008) 24-31

[2] E.J. Mittemeijer, M.A.J. Somers, Thermochemical surface engineering of steels, improving materials performance, 1st edition, Woodhead Publishing (2015)

[3] E.J. Mittemeijer, Fundamentals of nitriding and nitrocarburizing. In: ASM Handbook 4A: Steel Heat Treating Fundamentals and Processes, edited by J. Dossett and G.E. Totten, ASM Int., Materials Park, OH, USA (2013) 619-646

[4] K.H. Jack, Nitriding, Proc. Heat Treatment '73, The Metal Society, London, (1973) 39-50

[5] P.C. Van Wiggen, H.C.F. Rozendaal, E.J. Mittemeijer, The nitriding behaviour of iron-chromium-carbon alloys, Journal of Materials Science 20 (1985) 4561-4582

[6] C. Leroy, H. Michel, M. Gantois, Transformation of $(Cr,M)_7C_3$-type carbides during nitriding of chromium alloyed steels, Journal of Materials Science 21 (1986) 3467-3474

[7] J-N. Locquet, R. Soto, L. Barrallier, A. Charaï, Complete investigation of a nitrided layer for Cr alloy steel, Microscopy Microanalysis Microstructures 8 (1997) 335-352

[8] H. Oettel, G. Schreiber, Formation of residual stresses in the diffusion layer, Nitrieren und Nitrocarburieren, AWT Tagunsband (1991) 139-151

[9] L. Barrallier, J. Barralis, On origin of residual stresses generated by nitriding treatment on alloy steels, Proceedings of the 4th International Conference on Residual Stress, Baltimore, USA, Society for Experimental Mechanics Inc (1994) 498-505

[10] N.E. Vives Diaz, R.E. Schacherl, L.F. Zagonel, E.J. Mittemeijer, Infleunce of the microstructure on the residual stresses on nitrided iron-chromium alloys, Acta Materialia 56(6) (2008) 1196-1208

[11] S.J.B. Kurz, S.R. Meka, N. Schell, W. Ecker, J. Keckes, E.J. Mittemeijer, Residual stress and microstructure depth gradients in nitrided iron-based alloys revealed by dynamical cross-sectional transmission X-ray microdiffraction, Acta Materialia 87 (2015) 100-110

[12] L. Barrallier, V. Traskine, S. Botchenkov, Morphology of intergranular cementite arraus in nitrided chromium-alloyed steels, Materials Science Engineering A 393 (2005) 247-253

[13] S. Jegou, L. Barrallier, R. Kubler, Phase transformations and induced volume changes in a nitrided ternary Fe-3%Cr-0.345%C alloy, Acta Materialia 58 (2010) 2666-2676

[14] C.W. Kang, S.R. Meka, T. Steiner, R.E. Schacherl, E.J. Mittemeijer, Microstructural evolution of 31CrMoV9 steel upon controlled gaseous nitriding treatment, HTM J.Heat Treatm. Mat. 71(5) (2016) 181-190

[15] S. Jegou, L. Barrallier, R. Kubler, M.A.J. Somers, Evolution of residual stress in the diffusion zone of a model Fe-Cr-C alloy during nitriding, HTM J. Heat Treatm. Mat. 66(3) (2011) 135-142

[16] W. Daves, F.D. Fischer, Finite element simulation of the development of residual stresses during nitriding under consideration of the micromechanical and metallurgical processes, Materials Science Forum 163-165 (1994) 713–718

[17] P. Buchhagen, T. Bell, Simulation of the residual stress development in the diffusion layer of low alloy plasma nitrided steels, Computational Materials Science 7-8 (1996) 228–234

[18] P. Depouhon, J.M. Sprauel, M. Mailhé, E. Mermoz, Mathematical modeling of residual stresses and distortions induced by gas nitriding of 32CrMoV13 steel, Computational Materials Science 82 (2014) 178-190

[19] E. Lehrer, Iron-hydrogen-ammoniac balance, Z. Elektrochem. 36 (1930) 383-392

[20] C.A. Schneider, W.S. Rasband, K.W. Eliceiri , NIH Image to ImageJ: 25 years of image analysis", Nature methods 9(7) (2012) 671-675, PMID 22930834

[21] A.L. Christenson, E.S. Rowland, Residual stress in hardened high carbon steel, Transactions ASM 45 (1953) 638-676

[22] F. Bollenrath, V. Hauk, E.H. Muller, Zur Berechnung der vielkristallinen Elastizititskonstanten aus den Werten der Einkristalle, Z. Metallkde. 58 (1967) 76-82

[23] L. Castex, Redistribution des contraintes dans une plaque après enlèvement de matière, Groupement français pour l'analyse de contraintes par diffractométrie X (1984)

[24] M.G. Moore, W.P. Evans, Mathematical correction for stress in removed layers in X-ray diffraction residual stress analysis, SAE Transactions 66 (1958) 340-345

[25] D.H. Jack, P.C. Lidster, P. Grieveson, K.H. Jack, Kinetics of nitriding iron alloys, in Chemical Metallurgy of Iron and Steel, Iron and Steel Inst., London (1973) 374-376

[26] G.A. Thomas, J.G. Speer, D.K. Matlock, G. Krauss, R.E. Hackenberg, Time-temperature equivalence in martensite tempering, in International Conference on Martensitic Transformations (ICOMAT) (eds G. B. Olson, D. S. Lieberman and A. Saxena), John Wiley & Sons, Inc., Hoboken, NJ, USA (2010)

[27] J.D. Fast, M.B. Verrijp, Diffusion of nitrogen in iron, The Journal of the Iron and Steel Institute 176 (1954) 24-27

[28] J.R.G. da Silva, R.B. McLellan, Diffusion of carbon and nitrogen in B.C.C iron, Materials Science and Engineering 26 (1976) 83-87

[29] R. Angers, F. Claisse, Improvement of Kryukov and Zhukhovitskii method for measurement of diffusion. Application to self-diffusion in alpha iron, Canadian Metallurgical Quarterly 7(2) (1968) 73-78

[30] E.J.Mittemeijer, W.T.M. Straver, P.F. Colijn, P.J.van der Schaaf, J.A. van der Hoeven, The conversion cementite → ε-nitride during the nitriding of FeC-alloys, Scripta Metallurgica 14 (1980) 1189-1192

[31] C. Ginter, L. Torchane, J. Dulcy, M. Gantois, A. Malchere, C. Esnouf, T. Turpin, A new approach to hardening mechanisms in the diffusion layer of gas nitrided α-alloyed steels. Effects of chromium and aluminium : experimental and simulation studies, La Metallurgia Italiana 7-8 (2006) 29-35

[32] P. Jessner, M. Gouné, R. Danoix, B. Hannoyer, F. Danoix, Atom probe tomography evidence of nitrogen excess in the matrix of nitrided Fe-Cr, Philosophical Magazine Letters 90(11) (2010) 793-800

[33] S. Hoja, F. Hoffmann, H.-W. Zoch, S. Schurer, T. Tobie, K. Stahl, Entwicklung von prozessen zum tiefnitrieren von zahnrädern, HTM J.Heat Treatm. Mat. 70(6) (2016) 276-285

Temperature [°C]	Time [h]	Nitriding potential [$atm^{-1/2}$]	Composition at the gas-solid interface
480	5	3.65	(ε)$Fe_{2-3}N$
	30		
520	5		
	30		
550	2.5		
	5		
	30		
	5	0.33	(γ')Fe_4N
	30		
	30	0.79	
	30	13.77	(ε)$Fe_{2-3}N$

Table 1: Experimental conditions for gaseous nitriding of 33CrMoV12-9 steel. The composition of the material at the gas-solid interface is given according to the Lehrer diagram [16].

Figure 0.a

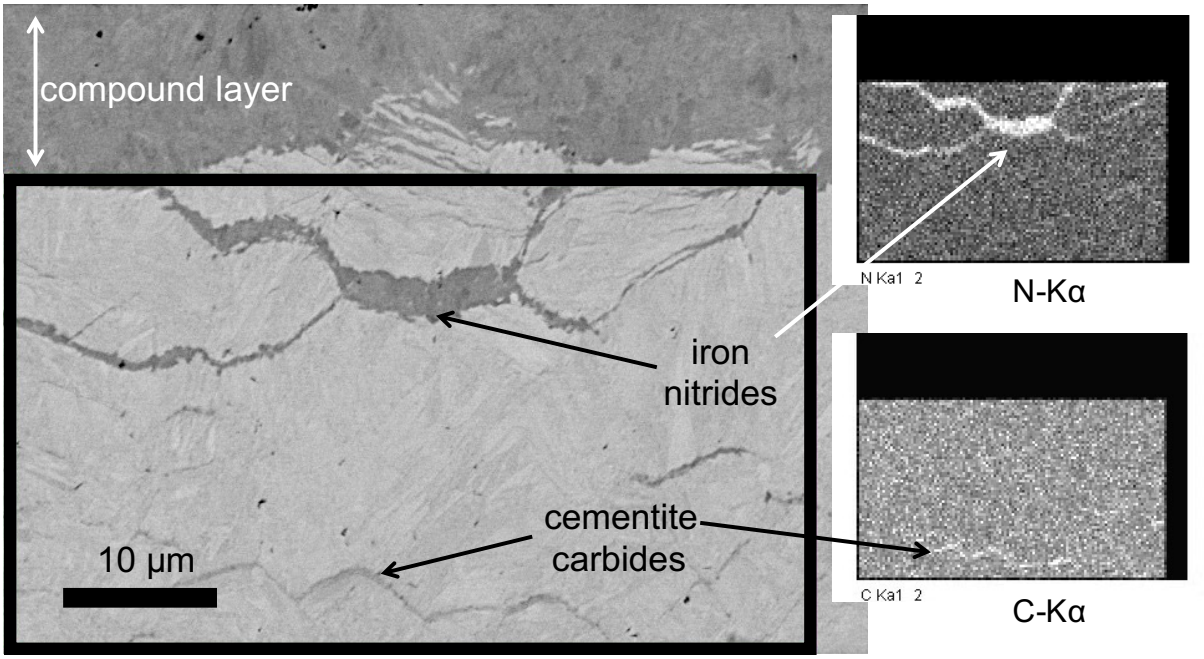

Figure 0.b

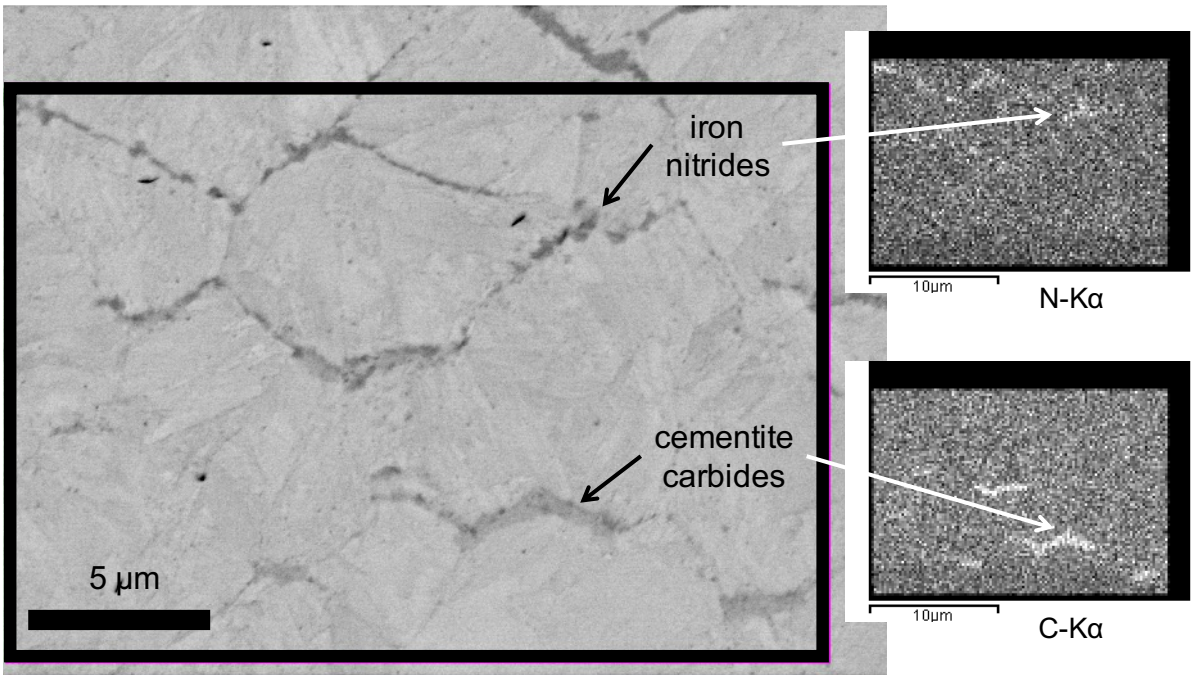

Figure 1

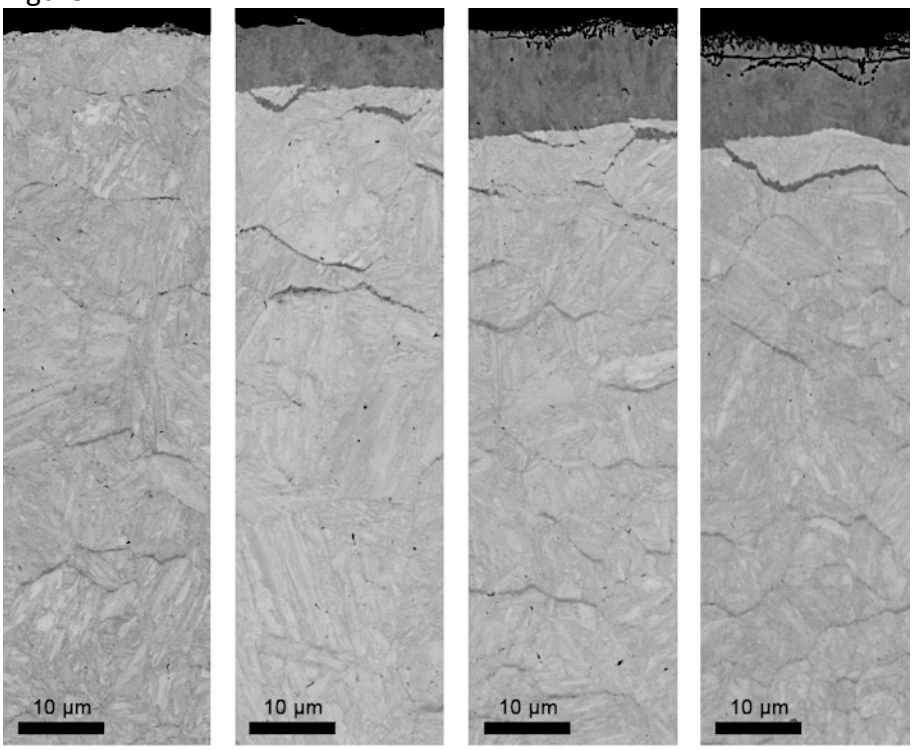

Figure 2

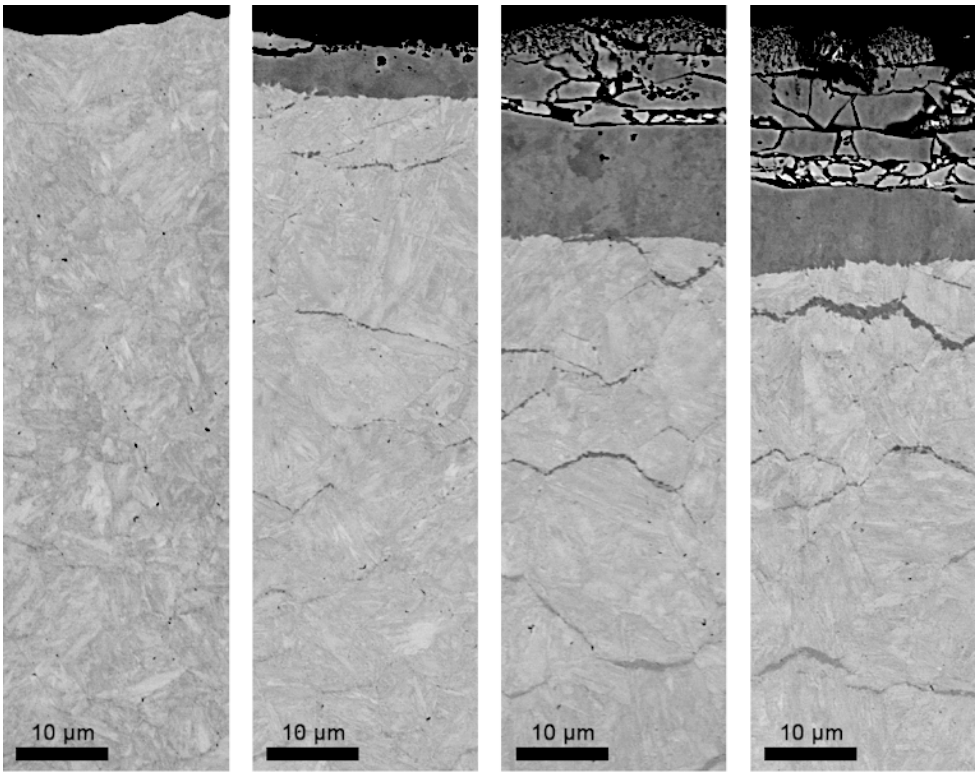

Figure 3

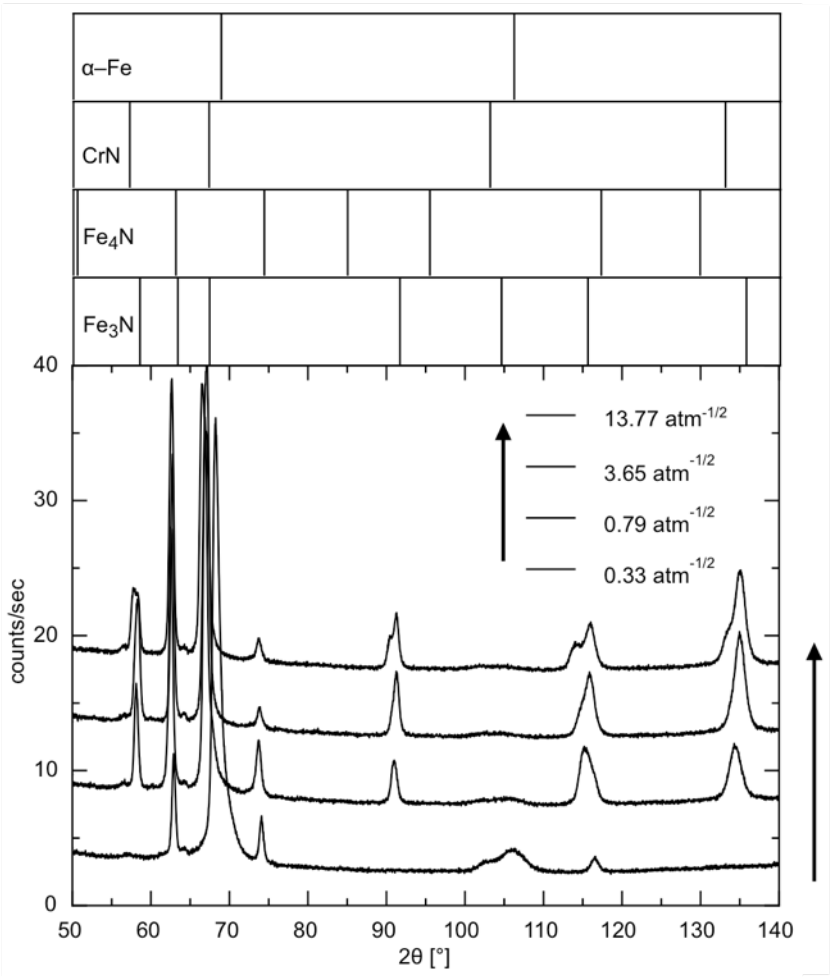
α–Fe
CrN
Fe4N
Fe3N
13.77 atm-1/2
3.65 atm-1/2
0.79 atm-1/2
0.33 atm-1/2
counts/sec
2θ [°]
0
10
20
30
40
50
60
70
80
90
100
110
120
130
140

Figure 4

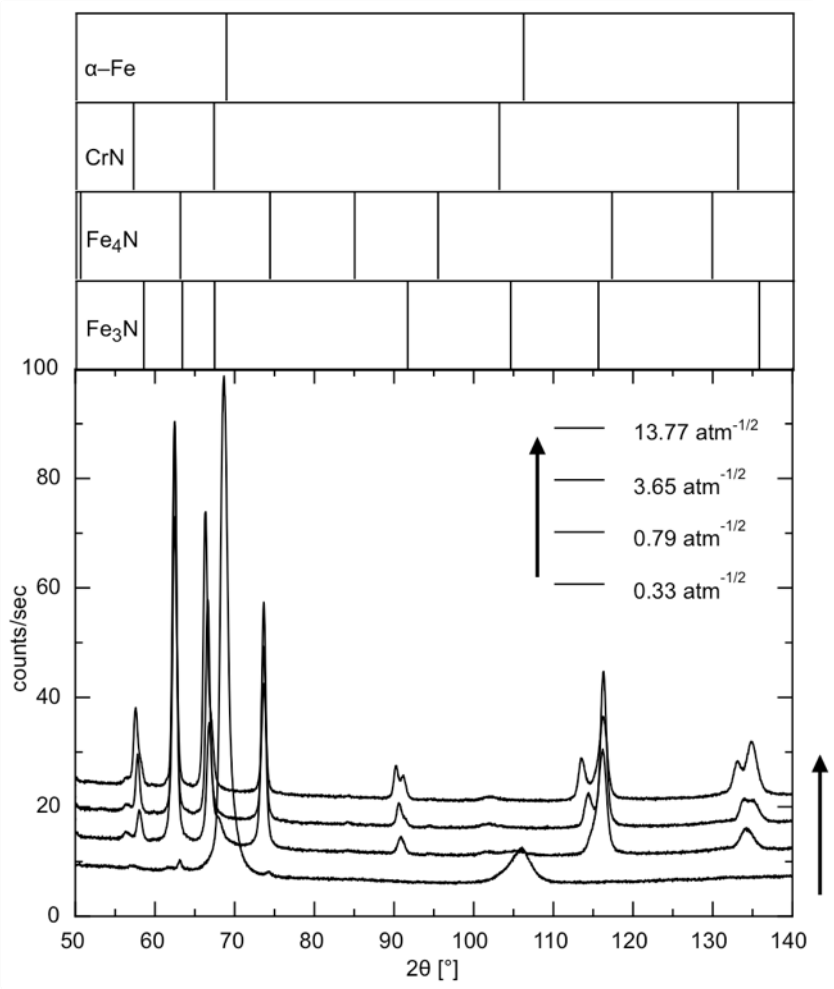
α–Fe
CrN
Fe4N
Fe3N
13.77 atm-1/2
3.65 atm-1/2
0.79 atm-1/2
0.33 atm-1/2
counts/sec
2θ [°]
0
20
40
60
80
100
50
60
70
80
90
100
110
120
130
140

Figure 5

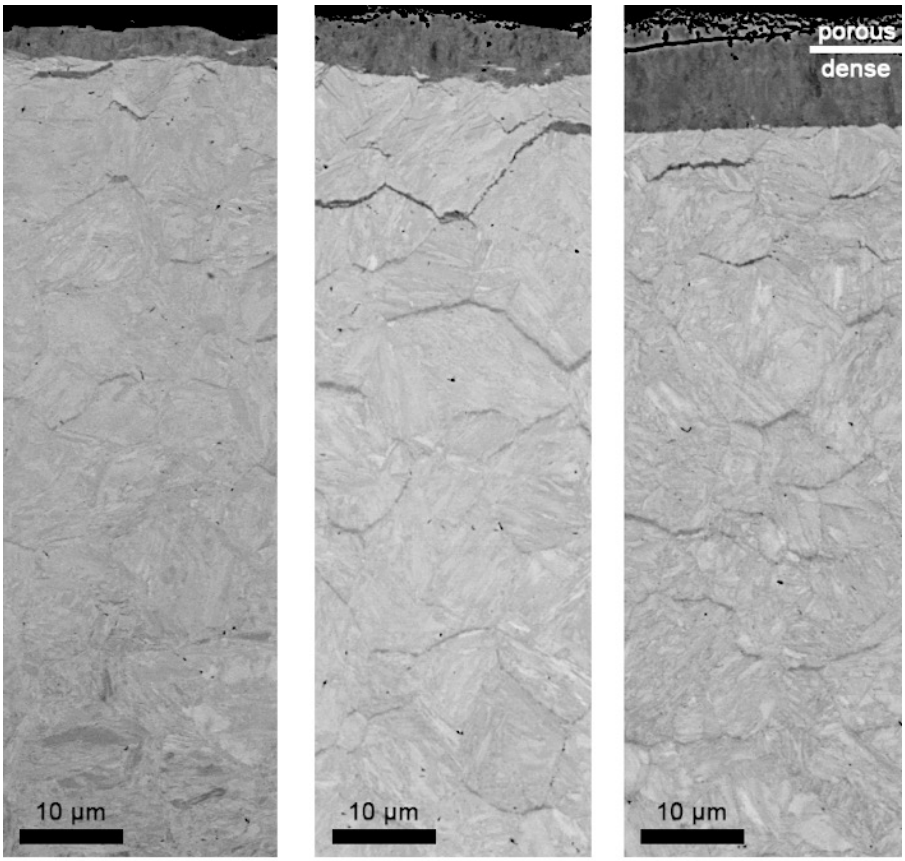

Figure 6

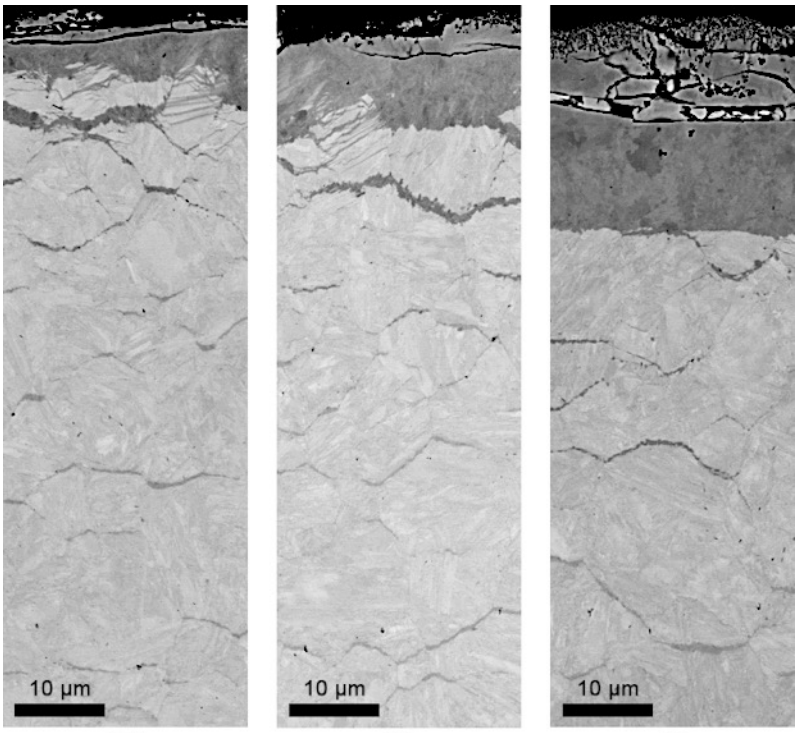

(a) (b) (c)

Figure 7

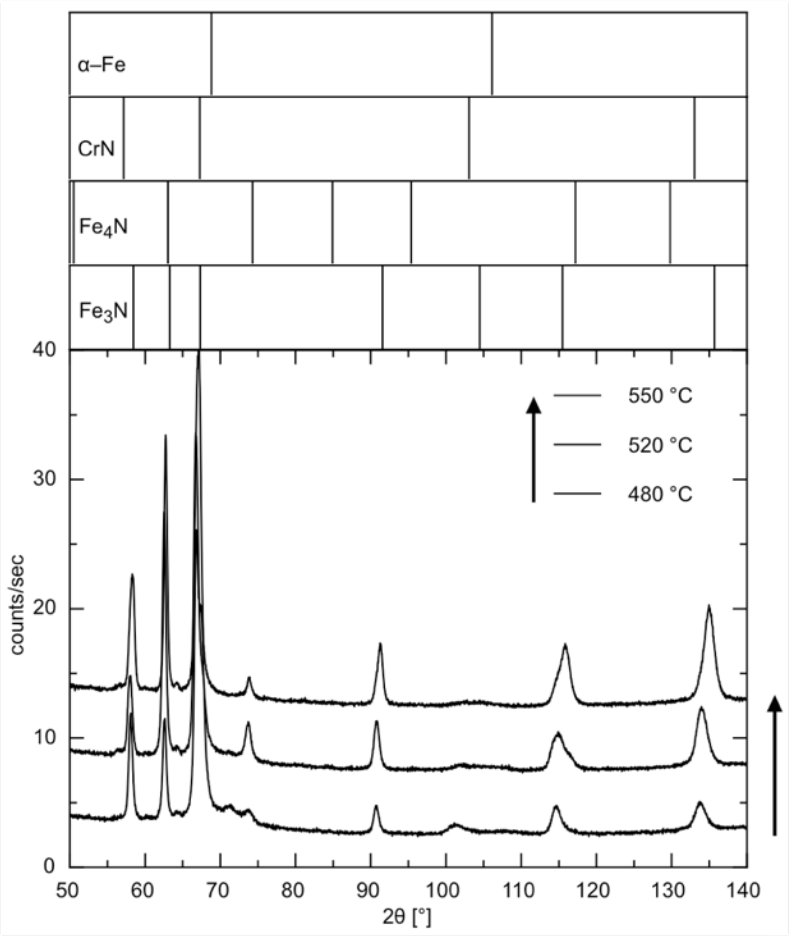
α–Fe
CrN
Fe4N
Fe3N
550 °C
520 °C
480 °C
counts/sec
2θ [°]
0
10
20
30
40
50
60
70
80
90
100
110
120
130
140

Figure 8

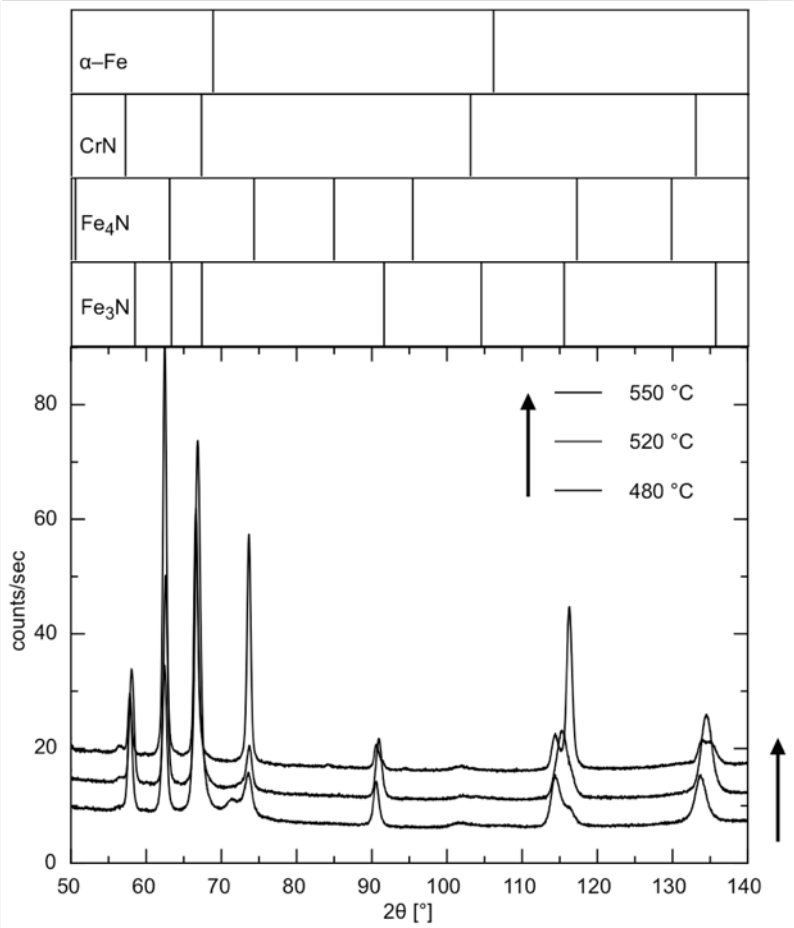
α–Fe
CrN
Fe4N
Fe3N
550 °C
520 °C
480 °C
counts/sec
2θ [°]
0
20
40
60
80
50
60
70
80
90
100
110
120
130
140

Figure 9

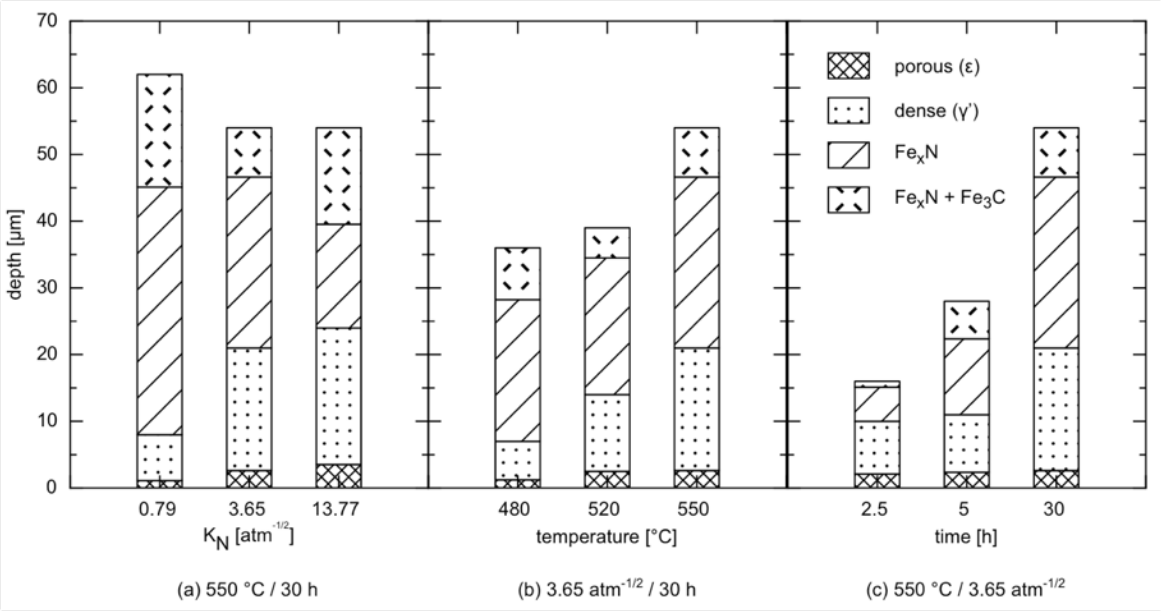
depth [µm]
70
60
50
40
30
20
10
0
0.79
3.65
13.77
K_N [atm$^{-1/2}$]
480
520
550
temperature [°C]
2.5
5
30
time [h]
porous (ε)
dense (γ')
Fe_xN
$Fe_xN + Fe_3C$
(a) 550 °C / 30 h
(b) 3.65 atm$^{-1/2}$ / 30 h
(c) 550 °C / 3.65 atm$^{-1/2}$

Figure 10

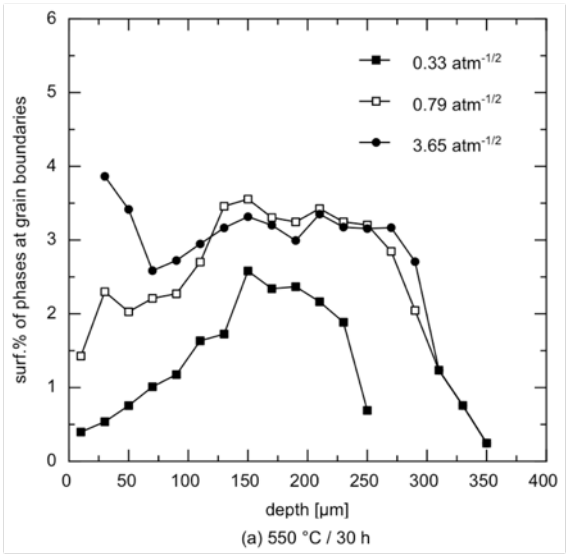
surf.% of phases at grain boundaries
depth [µm]
0.33 atm-1/2
0.79 atm-1/2
3.65 atm-1/2
(a) 550 °C / 30 h

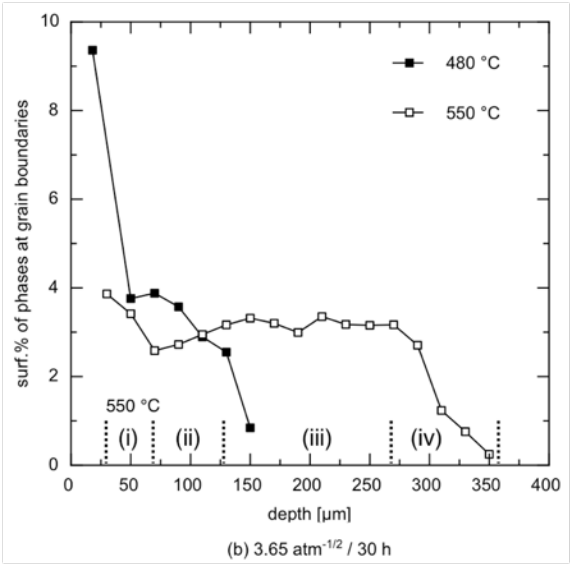
surf.% of phases at grain boundaries
depth [µm]
480 °C
550 °C
550 °C
(i)
(ii)
(iii)
(iv)
(b) 3.65 atm-1/2 / 30 h

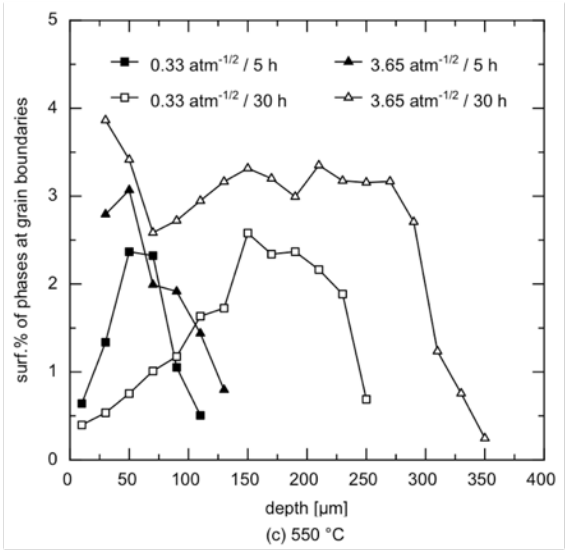
surf.% of phases at grain boundaries
depth [µm]
0.33 atm-1/2 / 5 h
0.33 atm-1/2 / 30 h
3.65 atm-1/2 / 5 h
3.65 atm-1/2 / 30 h
(c) 550 °C

Figure 11

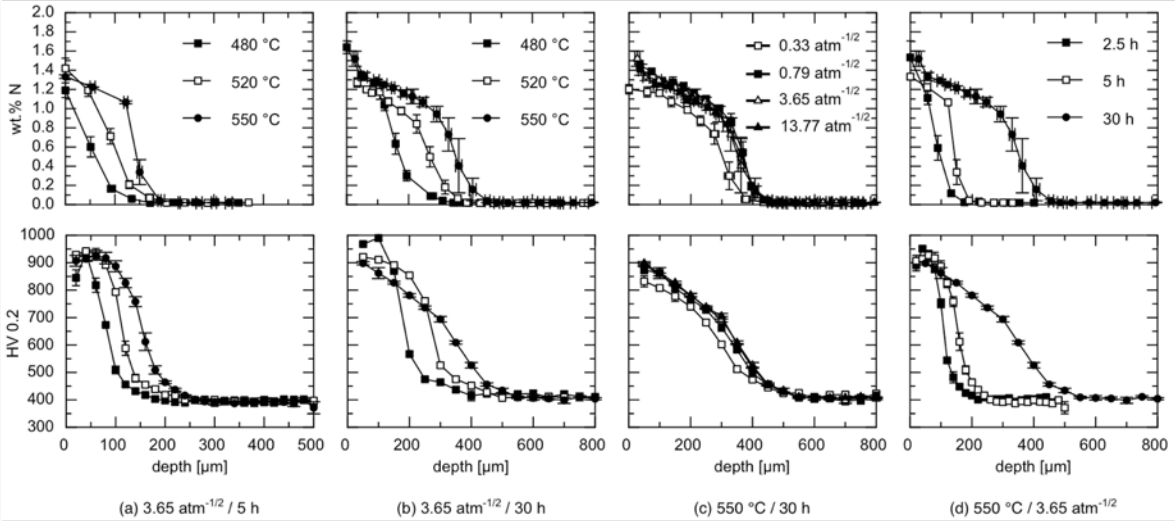
wt.% N
HV 0.2
480 °C
520 °C
550 °C
0.33 atm-1/2
0.79 atm-1/2
3.65 atm-1/2
13.77 atm-1/2
2.5 h
5 h
30 h
depth [µm]
(a) 3.65 atm-1/2 / 5 h
(b) 3.65 atm-1/2 / 30 h
(c) 550 °C / 30 h
(d) 550 °C / 3.65 atm-1/2

Figure 12

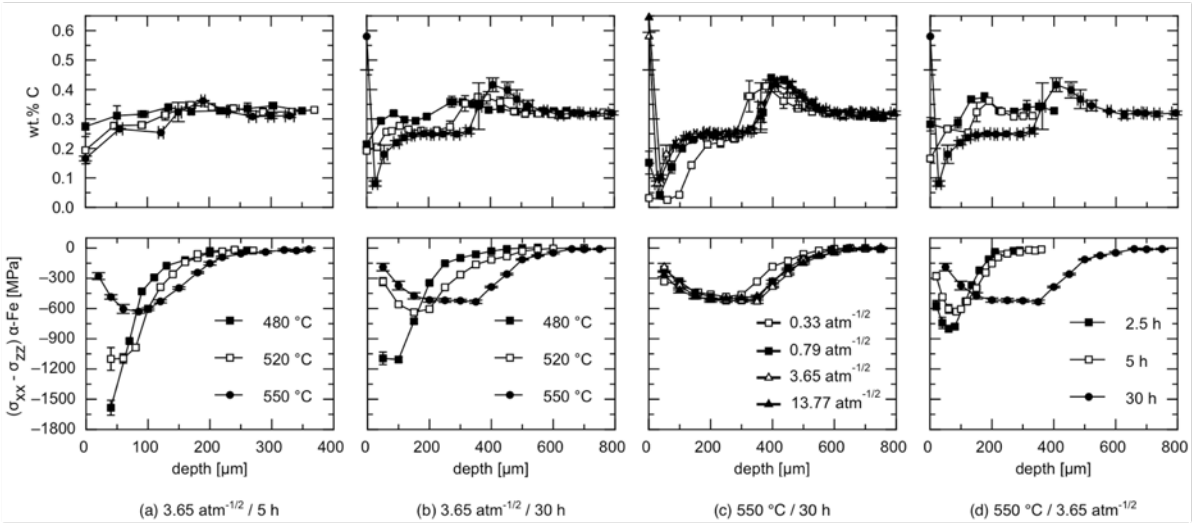
wt.% C
0.6
0.5
0.4
0.3
0.2
0.1
0.0
$(\sigma_{xx} - \sigma_{zz})$ α-Fe [MPa]
0
−300
−600
−900
−1200
−1500
−1800
480 °C
520 °C
550 °C
0.33 atm$^{-1/2}$
0.79 atm$^{-1/2}$
3.65 atm$^{-1/2}$
13.77 atm$^{-1/2}$
2.5 h
5 h
30 h
depth [µm]
(a) 3.65 atm$^{-1/2}$ / 5 h
(b) 3.65 atm$^{-1/2}$ / 30 h
(c) 550 °C / 30 h
(d) 550 °C / 3.65 atm$^{-1/2}$

Figure 13

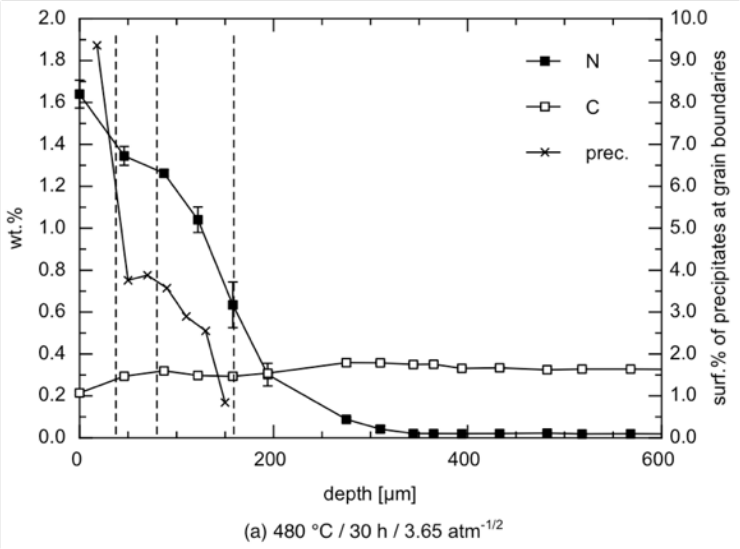

(a) 480 °C / 30 h / 3.65 $atm^{-1/2}$

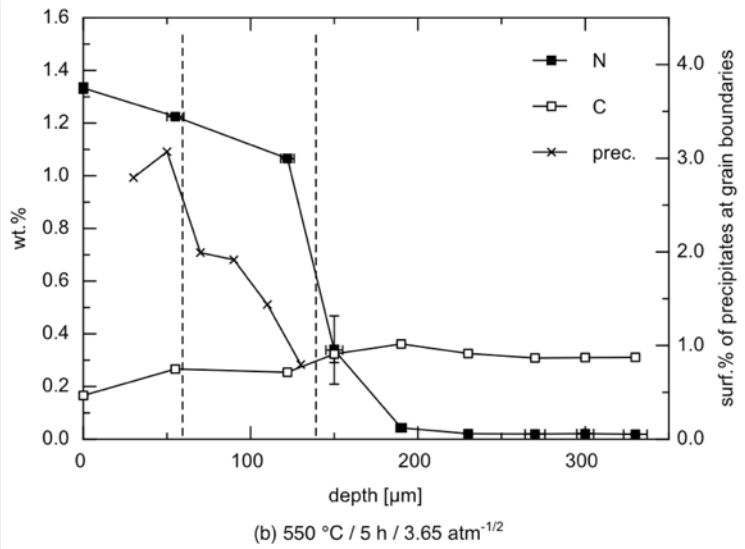

(b) 550 °C / 5 h / 3.65 $atm^{-1/2}$

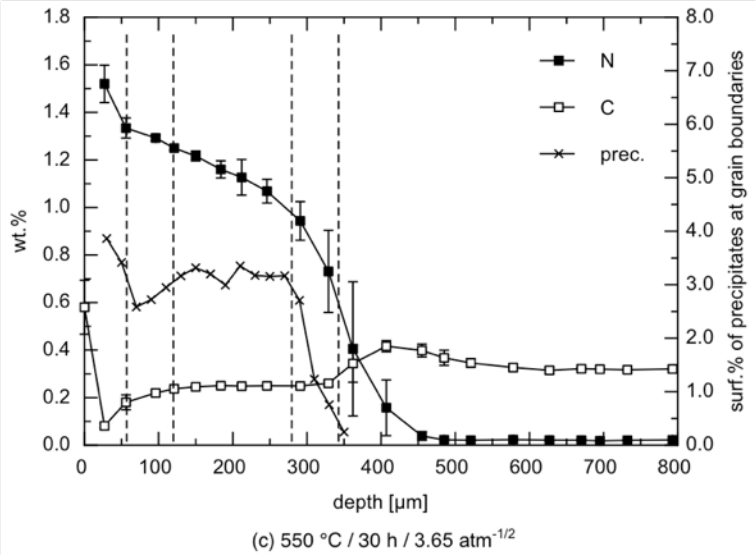

(c) 550 °C / 30 h / 3.65 $atm^{-1/2}$

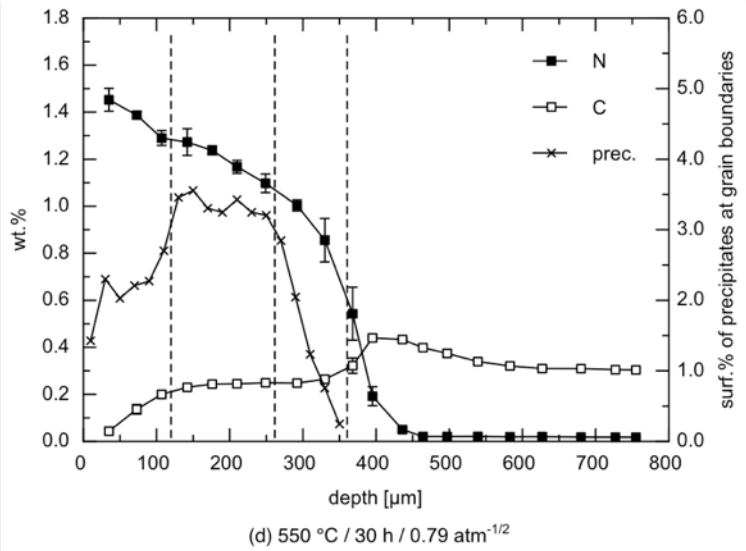

(d) 550 °C / 30 h / 0.79 $atm^{-1/2}$

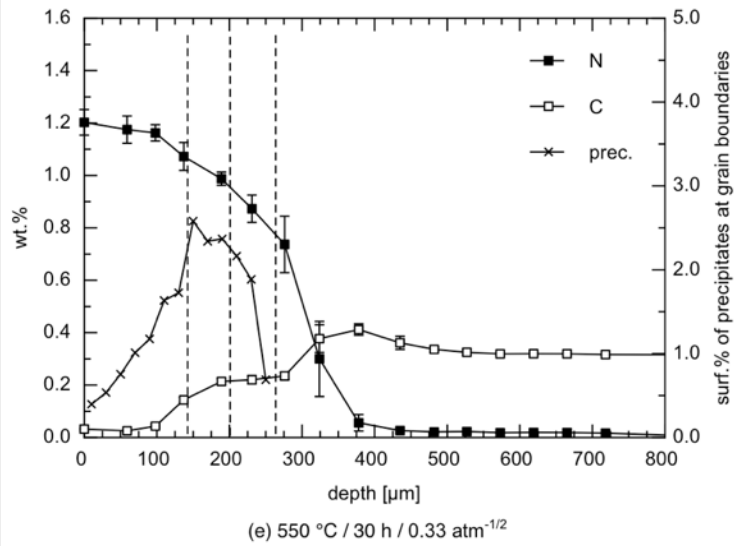

(e) 550 °C / 30 h / 0.33 $atm^{-1/2}$

Figure 14

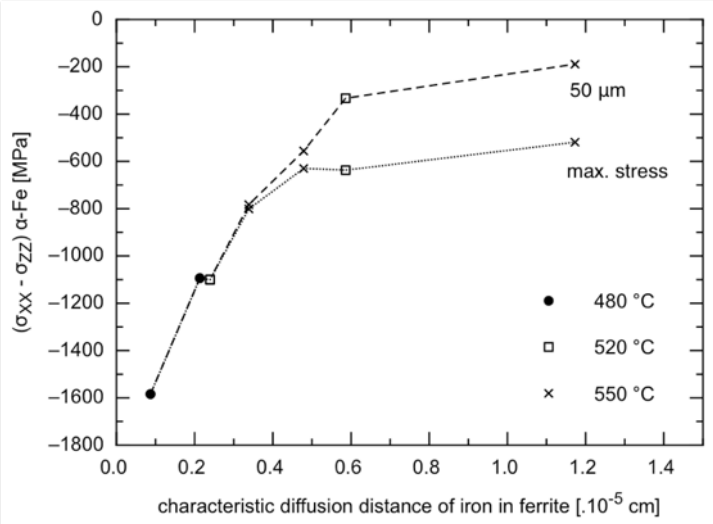
0
−200
−400
−600
−800
−1000
−1200
−1400
−1600
−1800
(σXX - σZZ) α-Fe [MPa]
50 µm
max. stress
480 °C
520 °C
550 °C
0.0
0.2
0.4
0.6
0.8
1.0
1.2
1.4
characteristic diffusion distance of iron in ferrite [.10-5 cm]

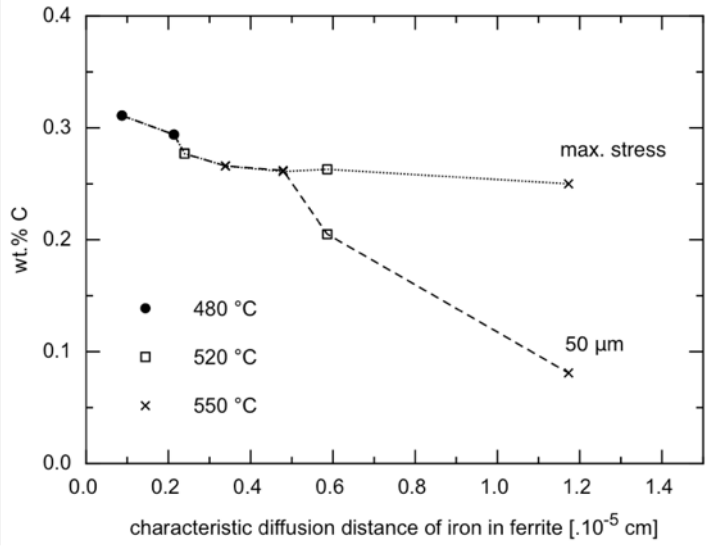
0.4
0.3
0.2
0.1
0.0
wt.% C
max. stress
480 °C
520 °C
550 °C
50 µm
0.0
0.2
0.4
0.6
0.8
1.0
1.2
1.4
characteristic diffusion distance of iron in ferrite [.10-5 cm]

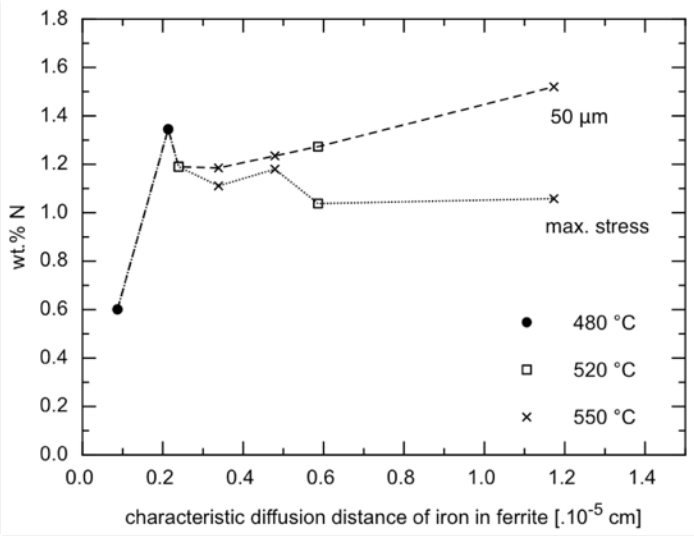
1.8
1.6
1.4
1.2
1.0
0.8
0.6
0.4
0.2
0.0
wt.% N
50 µm
max. stress
480 °C
520 °C
550 °C
0.0
0.2
0.4
0.6
0.8
1.0
1.2
1.4
characteristic diffusion distance of iron in ferrite [.10-5 cm]